

An infrared thermography-based method for the evaluation of the thermal response of tooling for composites manufacturing

Navid Zobeiry , John Park and Anoush Poursartip

Journal of Composite Materials
2019, Vol. 53(10) 1277–1290
© The Author(s) 2018
Article reuse guidelines:
sagepub.com/journals-permissions
DOI: 10.1177/0021998318798444
journals.sagepub.com/home/jcm



Abstract

The manufacture of large complex aircraft structures made of advanced composites is done by heating the parts on complex, thermally massive tools using convective heating inside autoclaves. In recent years, numerical simulation of the process has shown great value, but lack of knowledge of the convective heat transfer boundary conditions remains a major obstacle to widespread adoption. An infrared thermography method is presented, suitable for evaluating the thermal response of these processing conditions. The method is based on increasing the emissivity of a tool surface with a painted vacuum bag before thermal imaging. Accurate readings with an average temperature difference of 1.1°C compared to thermocouple data were achieved. The benefit of the thermography method is the highly detailed surface temperature map. Three tools with very similar geometries but made of Invar, aluminum and carbon fibre composite, respectively, were tested, and results interpreted using analytical solutions for the different tooling feature and convective boundary condition combinations. Analytical simulations, which were validated by comparison to numerical models, explain well the effect of autoclave airflow, tooling material and sub-structure variation on the temperature profiles measured by this infrared thermography method.

Keywords

Infrared imaging, advanced composites, autoclave processing, out-of-autoclave processing, tooling

Background and introduction

Given the promise of lighter and more efficient designs, application of advanced composites across many industries has enjoyed tremendous growth in the past decade. The successful application of carbon-fiber composites in commercial jetliners such as the Boeing 787 has paved the road for other industries to follow. The transition to composites, however, has not been a smooth ride and cost over-runs and schedule production delays are not uncommon. Unlike their metallic counterparts, for composites, the end quality is highly intertwined with the fabrication process. In recent years, to reduce risk, increasing emphasis has been placed on numerical simulation of these fabrication processes rather than relying on know-how, empirical knowledge, and trial-and-error exercises.¹ Process simulation of thermal management problems has been shown to be highly useful when dealing with composites fabrication.^{2,3} However, lack of knowledge of the boundary conditions including heat transfer coefficients (HTCs) remains a major obstacle to widespread adoption.

During the cure stage, a thermoset matrix composite part typically starts as a collated stack of raw, compliant material and develops into a rigid structure capable of sustaining loads. A well-controlled thermal cycle is a key requirement for successful processing. Numerous studies have shown that loss of control of process parameters results in a cascading list of part quality concerns, including: under-cure or over-cure (including possible thermal degradation due to exotherm), porosity, wrinkle growth, and excessive residual stress leading to the development of micro-cracks and/or dimensional changes.^{1–9}

In convective heating processes, the operator has control over the air temperature in hopes that the

Composites Research Network, Department of Materials Engineering, University of British Columbia, Canada

Corresponding author:

Navid Zobeiry, Composites Research Network, Department of Materials Engineering, University of British Columbia, 309-6350 Stores Road, Vancouver, BC V6T 1Z4, Canada.
Email: navid@composites.ubc.ca

part temperature follows through. However, due to thermal resistances of the system, part temperature lags behind the air temperature. In practice, material vendors recommend a cure cycle for their materials (commonly referred to as the Manufacturers Recommended Cure Cycle (MRCC)) with little guidance as to the limitations of applicability. It is well known in industrial circles that these MRCCs are merely the starting point for an acceptable cure cycle. As the laminate becomes thicker, tooling more complex, and equipment larger, the importance of a systems-based thermal design approach becomes increasingly more important. These cure cycles have to be designed not just around the material but around the entire curing system. A wide body of literature studying various components of the curing system now exists (e.g. see literature^{10–15}). This paper discusses the response of tooling and curing equipment.

The cure tooling, by mass, is greater than that of the actual composite part, and this ratio increases rapidly with increasing part size. Consequently, the tool will have a strong influence on the thermal response of the material in most parts of industrial significance. Given this consideration, tooling material selection and geometry design become important factors in the thermal management of the part.

The curing equipment is often in the form of a gas (typically nitrogen) pressurized autoclave or unpressurized oven; in either case, these systems rely on convective heat transfer. This form of heat transfer is characterized by the HTC which is correlated to the local flow velocity over a tool. For constant flow velocity conditions and simple geometries, the HTC can be analyzed with respect to the gas properties and velocity (e.g. see Bergman et al.¹⁶). This, however, has limited applicability since most industrial cases have complex geometries and flows and it is non-trivial to determine HTC values.

HTC values in autoclaves and ovens are often characterized using lumped mass calorimeters. For example, Ghariban et al.¹⁷ measured highly turbulent flows within an autoclave environment using a copper plate calorimeter to measure variations in HTC along the length of an autoclave. Johnston et al.¹⁸ developed a model to account for HTC increases with curing pressure and Hudek et al.¹⁹ extended this model to include variation along the length of the curing equipment. Recent work from Weber et al.²⁰ includes the effects of inter and intra-part shadowing effects observed in batch loading conditions. Maffezzoli and Grieco²¹ among others, demonstrate that how knowledge of the heating relationship between a tool and equipment can result in operational efficiencies through cure time reduction using the simulation tools. All of these studies used instrumented thermocouples or calorimeters to assess temperature and HTCs.

These methods give high-resolution data for a spatially fixed location but do not give much information regarding temperature and HTC variation across the curing vessel. It can be said that these types of measurements are 0D measurements offering a point or locally averaged assessment of the temperature or HTC.²² IR thermography provides an alternative approach for the evaluation of a curing system. Although this method has been used extensively in various applications (e.g. see Carlomagno and Cardone²² and Goidescu et al.²³), only a few attempts have been made to implement this method for evaluating composites curing systems. For example, infrared imaging was recently utilized in various autoclave operations.^{24–26} In these studies, an infrared camera installed inside an autoclave monitored temperature variations. In another study, flow front progression in resin infusion using IR imaging was investigated.²⁷

IR thermography of composites curing processes is affected by the radiation from the surroundings of the part, including reflected radiation from the curing equipment. This requires implementation of proper calibration procedures to improve accuracy of the readings (e.g. see Ucan et al.²⁷). However, even with proper calibration, the high reflectivity of metallic tools (e.g. aluminum or Invar) limits the application of IR thermography to monitor a curing system.

To address this issue, a method has been developed and proposed in this paper. Combined with a proper calibration procedure, temperature measurement with high accuracy was achieved. In this method, the surface of the tool is covered with a vacuum bag painted black to increase the emissivity of the tool surface. This method is used to analyze the thermal response of three tools with similar geometries but with different tooling materials (Invar, aluminum and composite). Using these results combined with analytical and numerical solutions, several parameters were identified as influencing the thermal response: autoclave airflow variation, tooling material and tooling sub-structure. The proposed method provides a continuous representation of temperature on a tool and can be potentially used to evaluate the composite curing systems.

Thermal behaviour of a curing system

This study considers three tools of nominally identical surface geometry. Each tool is constructed with a different material: Carbon fiber-reinforced polymer composite (CFRP), aluminum 6061-T6, and Invar 36. These materials are representative of conventional tooling systems in composites processing. The nominal dimensions of these tools are 0.8 m wide \times 1.2 m long \times 0.48 m high. The metallic tools are constructed with nominal 12.7 mm thickness plate (facesheet and sub-structure) and the

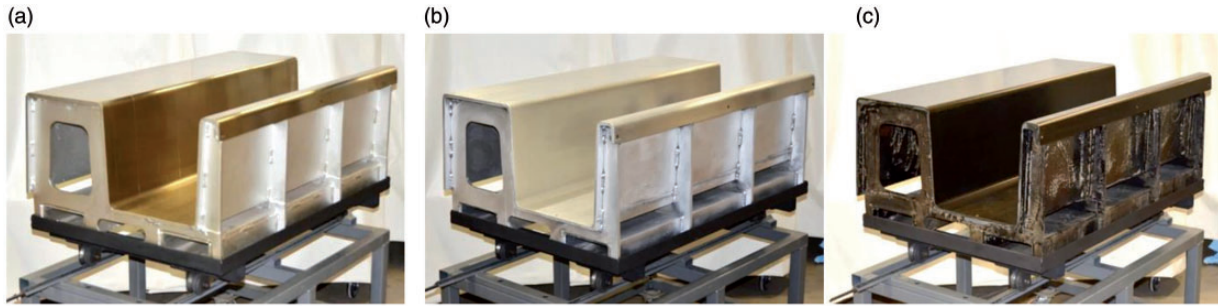


Figure 1. Three tools with similar geometries of 1.2 m × 0.8 m × 0.48 m but with different tooling materials of Invar 36 (a), Aluminum 6061-T6 (b) and CFRP composite (c).

Table 1. Material properties for the three tools used in this study.

Dimensions/properties	Invar 36	Aluminum 6061-T6	CFRP Composite
Nominal dimensions L × W × H (m)	1.2 × 0.8 × 0.48	1.2 × 0.8 × 0.48	1.2 × 0.8 × 0.48
Nominal facesheet Thickness (mm)	12.7	12.7	8.8
Nominal sub-structure Thickness (mm)	12.7	12.7	10
Density (kg/m ³)	8000	2700	1580
Total weight (kg)	400	135	50
In-plane conductivity (W/mK)	11	167	4.93 (at 20°C) 9.46 (at 180°C)
Through-thickness conductivity (W/mK)	11	167	0.47 (at 20°C) 0.51 (at 180°C)
Specific heat capacity (J/kgK)	515	896	962 (at 20°C) 1146 (at 180°C)

Note: Intrinsic properties are taken from Hubert²⁸ and Davis²⁹ consistent with the RAVEN software package.³⁰
CFRP: carbon-fiber reinforced polymer.

CFRP tool is constructed to a nominal 8.8 mm facesheet thickness and nominal 10 mm sub-structure thickness with localized thickness increases for the assembly and dimensional verification purposes. The three tools considered in this study are shown in Figure 1. Several properties of the tool are presented in Table 1. Thermal properties are assumed to be nominal material properties and representative of these tooling systems.

The vessel used for this study is a 1.15 m diameter × 1.5 m length autoclave produced by the American Autoclave Company. The autoclave is PLC controlled and interfaced via programmable cure recipes using vendor provided computer software. Heating and cooling are supplied by a 40 kW resistive heating system and cooled using facility supplied water. Air circulation is fan driven by a 30 kW induction motor from the rear of the autoclave and floor ducted to the front of the vessel before entering the operating envelope of the autoclave. Autoclave airflow characterization was previously performed by Slesinger et al.³¹ Maximum flow velocity is observed at the top of the vessel and decreases toward

the bottom of the autoclave. Within 0.5 m of the door, the flow stagnates and toward the bottom of the vessel, the flow is observed to reverse in direction.

IR thermography method

Theory

In infrared thermography, the total radiation received by the sensor, W_{tot} , comes from three sources: radiation from the object, W_{obj} , reflected radiation from the surroundings of the object, W_{ref} and radiation from the atmosphere, W_{atm} .^{32–34} This can be described using the following equation

$$W_{tot} = W_{obj} + W_{ref} + W_{atm} \quad (1)$$

This equation can be expanded as follows

$$W_{tot} = \varepsilon\tau\sigma T_{obj}^4 + (1 - \varepsilon)\tau\sigma T_{ref}^4 + (1 - \tau)\sigma T_{atm}^4 \quad (2)$$

where σ is the Stefan–Boltzmann constant equal to $5.67 \times 10^{-8} \frac{W}{m^2 K^4}$, ε is the emissivity of the object, τ is the atmosphere transmittance parameter, T_{obj} is the temperature of the object, T_{ref} is the temperature of the surroundings of the object reflected toward the camera and T_{atm} is the temperature of the atmosphere. For reflective metallic tools such as aluminum, the emissivity is very low ($\varepsilon < 0.1$). Based on equation (2), this significantly reduces the radiation from the object while increasing the reflected radiation from the surroundings. Such low emissivity can potentially affect the accuracy of readings. To overcome this

problem, the surface is covered with a painted vacuum bag to increase its surface emissivity. The method is described in the next section.

Method

Each tool was initially cleaned using isopropyl alcohol. Once cleaned, 15 thermocouples were attached on the tool surface using heat-resistant tape at equal intervals. Locations of thermocouples are schematically depicted in Figure 2. Once the thermocouples were attached, the tool surface was covered with a layer of nylon peel ply

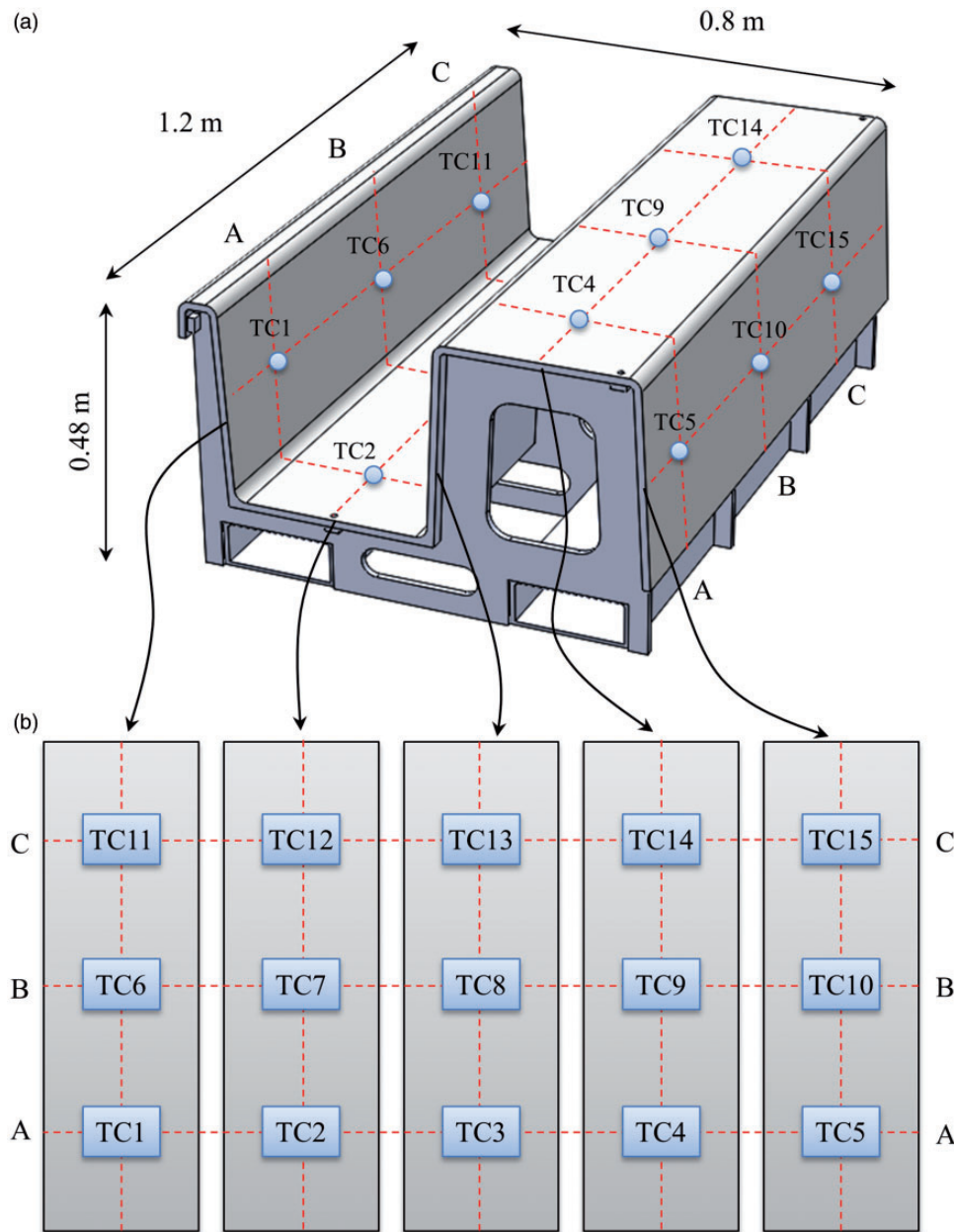


Figure 2. Schematic of locations of 15 thermocouples on the tool surface: (a) Tool isometric view and (b) tool flatten top view.

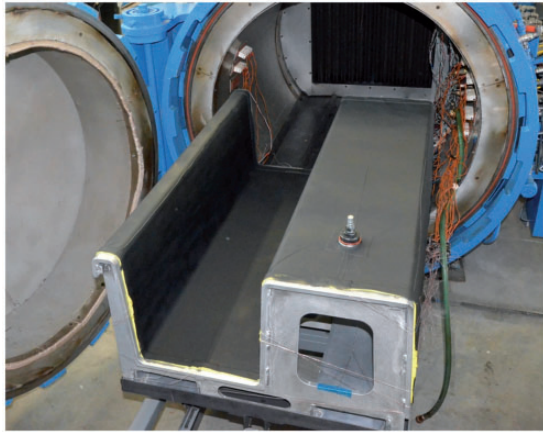


Figure 3. A tool covered with a painted vacuum bag before loading into the autoclave.

(Airtech Bleeder Lease B). A nylon vacuum bag (Stretch-VAC 2000) with a vacuum port was then placed and sealed on the tool surface using the sealant tape. After applying vacuum, the vacuum bag was spray painted using a black matte paint (KRYLON 44290). An image of a tool prepared using the described process is also shown in Figure 3.

The prepared tools were heated in the autoclave at atmospheric pressure. For each test, the autoclave temperature was increased from room temperature to 100°C at a constant heating rate of 5°C/min. After reaching 100°C, the autoclave was turned off, the tool was quickly rolled out and the autoclave opening was covered with cardboard before imaging. This was done to minimize radiation from the vessel. Additional tests were also conducted with different dwell times at 100°C. IR images were taken using an FLIR T620 IR Camera with a 13.1 mm wide lens. The total time from turning off the autoclave to taking images was kept around 1 min to minimize the heat loss. During the entire process including heat-up cycle, tool removal and IR thermography, the tool surface temperature was monitored using the thermocouples for verification and collection of the transient temperature history.

Calibration process

In order to accurately measure the temperature of the tool surface (T_{obj}), several parameters were measured to calibrate the readings of the IR sensor: tool surface emissivity, reflected apparent temperature, atmospheric temperature, relative humidity, camera to object distance, and atmosphere transmittance.

Emissivity was measured using the commonly accepted heat-up method described in Minkina and Dudzik.³⁵ The emissivity of the black spray paint was found to be 0.98. The reflector method described in

Table 2. Calibration parameters for IR thermography.

Parameter	Value	Measurement method
Emissivity, ϵ	0.98	Heat-up method ³⁵
Reflected apparent temperature, T_{ref}	35°C	Reflector method ³³
Atmospheric temperature, T_{atm}	25°C	Thermometer
Relative humidity (RH%)	32%	Humidity meter
Camera to object distance	1.4 m	Measurement tape
Atmosphere transmittance	0.99	LOWTRAN Model ³⁵

IR: infrared.

FLIR Systems³³ was used to measure a reflected apparent temperature of 35°C. During each test, atmospheric temperature, relative humidity and camera distance to the object were also recorded using a thermometer and a humidity meter. Using these values and the LOWTRAN model described in Minkina and Dudzik,³⁵ the atmosphere transmittance was estimated. Considering the short distance of camera to object (~1.4 m), a high value of 0.99 was estimated for atmosphere transmittance. All calibration parameters are reported under Table 2.

Experimental results

An IR image taken from the surface of the Invar tool after the heat-up cycle is shown in Figure 4. Thermal variation is observed due to two conditions: autoclave airflow variation and tooling sub-structure. The effect of tooling sub-structure is observed directly over, and near, sub-structure attachment locations creating localized cold spots with a minimum temperature of 40.6°C. High airflow conditions can be observed toward the rear of the tool as a result of the previously reported airflow pattern in this autoclave creating a hot spot with a maximum temperature of 57.5°C, while low airflow creates a cold spot with a minimum temperature of 43.6°C toward the front of the autoclave.

Comparative IR images taken from the surfaces of the three tools are presented in Figure 5. The Invar tool is the coldest tool with a maximum temperature of 57.5°C (i.e. highest thermal lag) and the composite tool is the hottest tool with a maximum temperature of 78.0°C (i.e. lowest thermal lag). The aluminum tool exhibits the least temperature gradient with no visible effect of the sub-structure. Maximum and minimum surface temperatures for each tool are listed under Table 3.

The thermocouple readings from each tool are compared in Figure 6. Detailed thermocouple measurements for the Invar tool are shown in Figure 7. The time of the tool removal from the autoclave and

IR thermography is marked. Analysis of TC data in Figure 7 shows a uniform cool-down once the tool is removed from the autoclave. At the time of IR thermography of the Invar tool about 1 min after tool removal, TC measurements show an average cool-down of 6.2°C with a standard deviation of 0.9°C.

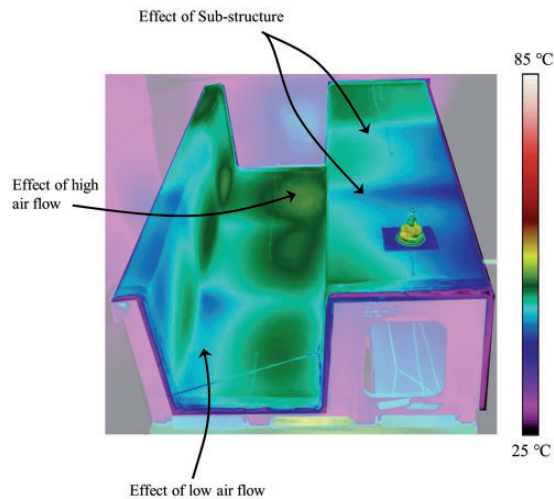


Figure 4. IR image of the Invar tool surface immediately after a heating cycle of 5°C/min to 100°C. IR: infrared.

Similar uniform trends were observed for the composite and aluminum tools. This implies that the temperature gradients observed using IR thermography is a representation of the gradients on the tool surface inside the autoclave. The comparison of readings in Figure 6 confirms that the composite tool is the hottest tool and the Invar tool is the coldest tool. IR thermography results were compared with the thermocouple readings and the average and maximum differences between two measurements are listed under Table 4. This shows an average difference of 1.1°C and a maximum difference of 3.3°C. It should be noted that the special limits of error (SLE) of type J thermocouples used in this study is $\pm 1.1^\circ\text{C}$.

Discussion

Observations from the IR experiments may be explained using the analytical solutions developed from an energy balance argument and validated numerically. Three key parameters influence the surface temperature variations: (1) autoclave airflow variation (2) tooling material and (3) sub-structure.

Effect of air flow variation

The resultant images in Figures 4 and 5 illustrate the full temperature distribution across the tool. Several

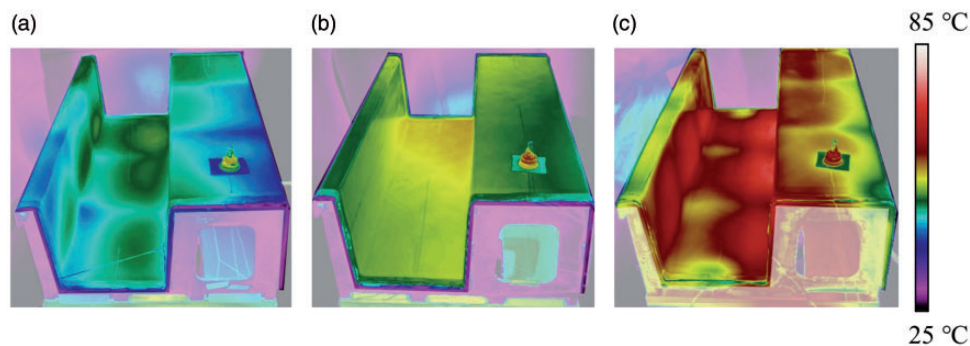


Figure 5. IR images of the surfaces of three tools immediately after a heating cycle of 5°C/min to 100°C: (a) Invar tool, (b) Aluminum tool and (c) CFRP tool.

IR: infrared; CFRP: carbon fiber-reinforced polymer.

Table 3. Comparison of the maximum and minimum surface temperatures for the three tools measured using the IR thermography method.

Tool	Maximum surface temperature (°C)	Minimum surface temperature (°C)	Max-min surface temperatures (°C)
Invar 36	57.5	40.6	16.9
Aluminum 6061-T6	64.4	51.3	13.1
CFRP Composite	78.0	51.9	26.1

Note: Tools were heated to 100°C with a heating rate of 5°C/min.

IR: infrared; CFRP: carbon fiber-reinforced polymer.

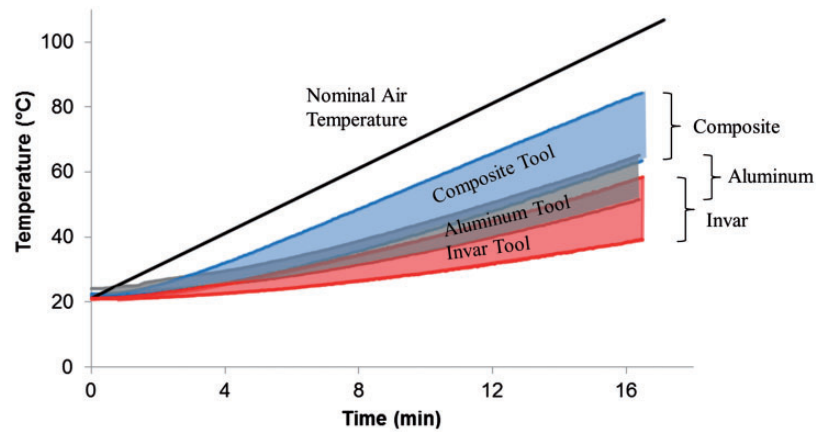


Figure 6. Comparison of the thermal envelope of tool surfaces from the thermocouple data for three tools subjected to a heating rate of 5°C/min.

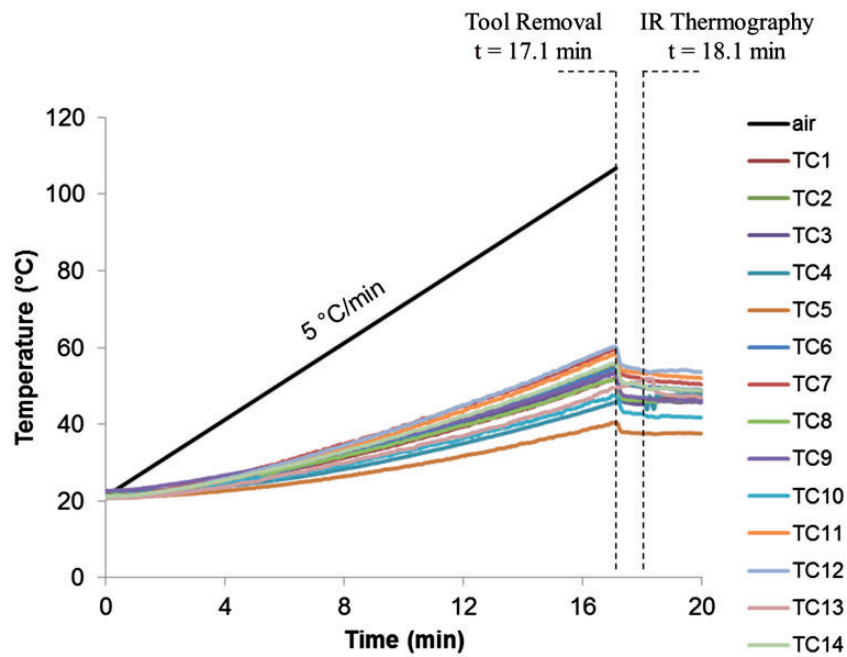


Figure 7. Thermocouple readings from the surface of the Invar tool subjected to a heating cycle of 5°C/min to 100°C.

Table 4. Average and maximum differences between the IR thermography results and thermocouple readings for the three tools.

Tool	Average deviation from thermocouple readings (°C)	Maximum deviation from thermocouple readings (°C)
Invar 36	0.0 ± 0.8	−1.6 (TC9 as shown in Figure 2)
Aluminum 6061-T6	$−0.1 \pm 2.1$	−3.3 (TC4 as shown in Figure 2)
CFRP composite	1.1 ± 1.6	+3.3 (TC1 as shown in Figure 2)

Note: Tools were heated to 100°C with a heating rate of 5°C/min.

IR: infrared; CFRP: carbon fiber-reinforced polymer.

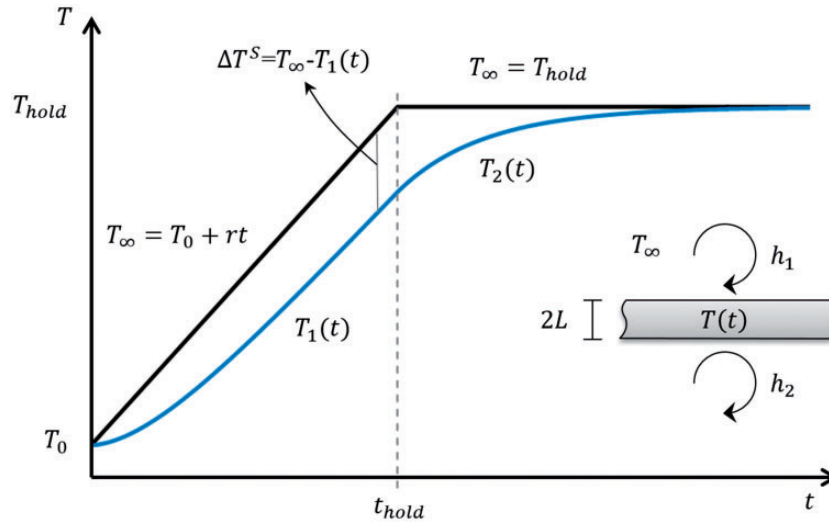


Figure 8. Representative transient response of a tool in convective heating subjected to a heat-up and hold cycle.

observations may be made regarding the effects of autoclave airflow variation. As observed by Slesinger et al.,³¹ the floor-ducted autoclave used in this study imparts a high-velocity plume near the top of the autoclave and near stagnant flows at the bottom of the autoclave toward the door. As the tools used in this study span this entire autoclave domain, the result is a significant variation of flow velocity across the tooling surface, creating localized hot spots toward the rear of the tool and cold spots near the front of the tool (i.e. coinciding with the high and low flow zones).

Consider a tool with a facesheet thickness of $2L$ in convective heating with HTC's of h_1 and h_2 as shown in Figure 8. During a heat-up cycle with a constant heating rate of r , and given enough time, the temperature of the tool reaches a quasi-steady-state with a constant thermal lag of ΔT . After the heat-up step ($t > t_{hold}$), the tool temperature approaches the constant hold temperature of T_{hold} . Considering HTC values for the atmospheric pressure of the autoclave used in this study ($HTC < \sim 50 \text{ W/m}^2\text{K}$ ³¹) and small Biot numbers ($Bi < 0.1$ for metallic tools and $Bi < 0.50$ for the composite tool), thermal responses of tools were approximated using the lumped mass assumption as follows (the full derivation may be found in Appendix 1, equation (11))

$$T(t) = \begin{cases} T_0 + rt - \Delta T^S(1 - e^{-\frac{r}{\Delta T^S}t}), & t < t_{hold} \\ T_{hold} - \Delta T^S(e^{-\frac{r}{\Delta T^S}(t-t_{hold})} - e^{-\frac{r}{\Delta T^S}t}), & t > t_{hold} \end{cases} \quad (3)$$

where ΔT^S is the quasi-steady-state thermal lag

$$\Delta T^S = r \frac{\rho C_P (2L)}{h_1 + h_2} \quad (4)$$

The effect of airflow variation is captured in equations (3) and (4) via the HTC's. As the flow increases, the HTC increases and the temperature lag decreases. Consequently, the local convective airflow and HTC's can now be realized by observing the surface temperature of the tool using IR thermography. The hottest locations have the highest airflow, while the coldest have the lowest flow.

For an Invar tool with properties listed under Table 1, two temperature profiles can be calculated for the minimum and maximum HTC conditions. Given a heating cycle at 5°C/min from room temperature to 100°C followed by a 70 min dwell time, the tool temperature was calculated using equation (3) and compared with the surface temperatures obtained numerically using the RAVEN software package³⁰ as shown in Figure 9. Calculations were performed for a hot spot with HTC's of $h_1 = 45 \text{ W/m}^2\text{K}$ and $h_2 = 15 \text{ W/m}^2\text{K}$ and a cold spot with HTC's of $h_1 = h_2 = 15 \text{ W/m}^2\text{K}$. IR thermography results obtained from three different tests are also superimposed on this figure. Comparison shows a near perfect match between the numerical and analytical solutions. Solutions are in good agreement with the measured range of temperatures from IR thermography results.

Effect of tooling material

For this experimental case, as the tool geometries and flow conditions are assumed to be identical, ρC_P become the only intrinsic material properties influencing the thermal lag as observed in equation (4). This means a thermally heavier tool, such as Invar, must be expected to show higher lag compared to the thermally lighter aluminum and CFRP variants.

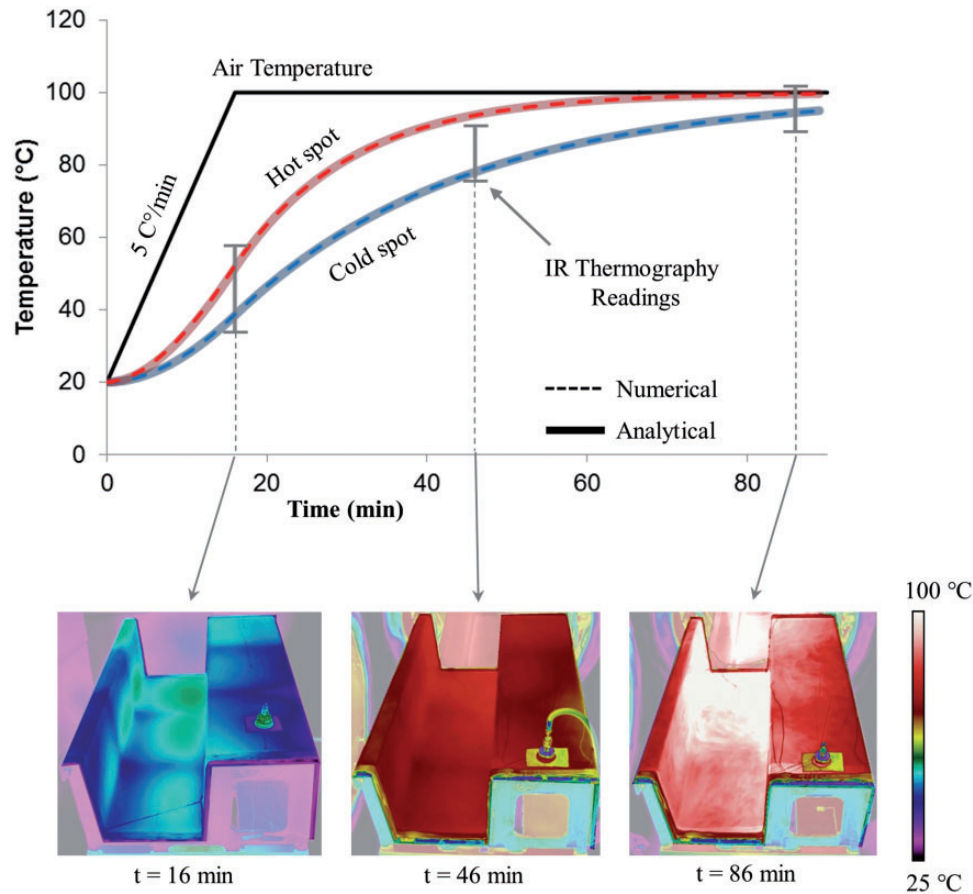


Figure 9. Comparison of the analytical, numerical and IR thermography results for transient thermal response of an Invar tool with properties listed under Table I. Analytical and numerical results are obtained for two locations: (1) a hot spot with HTC's of 45 W/m²K and 15 W/m²K and (2) a cold spot with an HTC's of 15 W/m²K. Numerical results were obtained using RAVEN.³⁰ IR images are obtained from three separate tests. Numerical and analytical results are nearly identical.

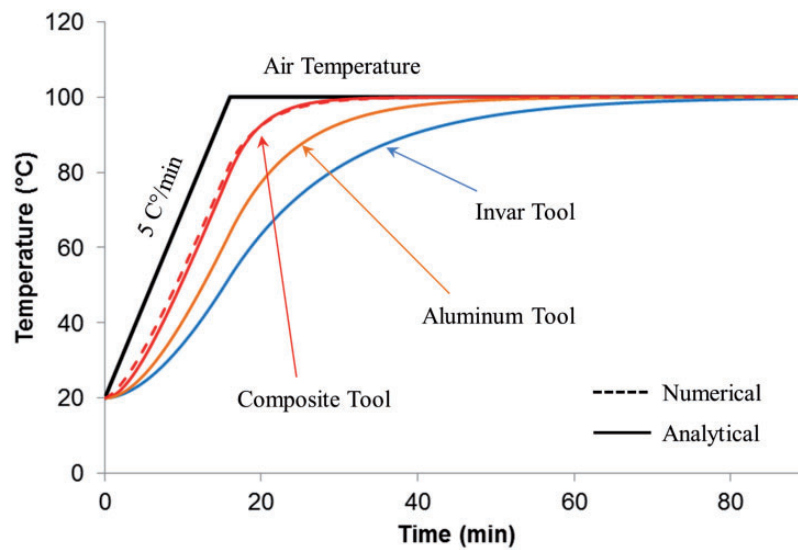


Figure 10. Transient thermal responses of three tools with properties listed under Table I with HTC's of 45 W/m²K and 15 W/m²K. Numerical results were obtained using RAVEN.³⁰ Analytical and numerical results are identical for metallic tools.

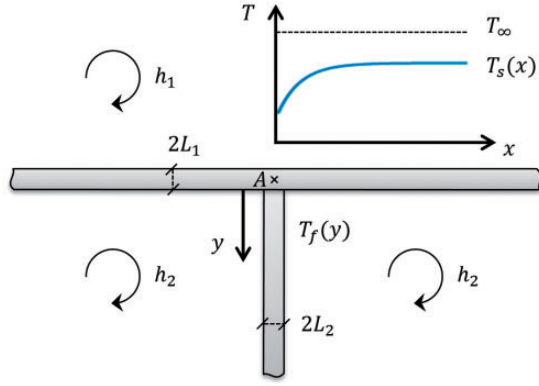


Figure 11. Schematic of a sub-structure attachment to the tool facesheet to create a localized cold spot.

Using the three tool types with properties listed under Table 1, for HTC of $h_1 = 45 \text{ W/m}^2\text{K}$ and $h_2 = 15 \text{ W/m}^2\text{K}$ and a heating rate of 5°C/min , temperatures were calculated using equation (3) and compared with the surface temperatures obtained numerically using RAVEN³⁰ (Figure 10). Before entering the hold temperature, the Invar tool predicts the highest lag at 47.8°C . Thermal lags in aluminum and composite tools were calculated as 36.1°C and 20.0°C , respectively. For the metallic tools that have very small temperature variation through thickness ($Bi < 0.1$), an excellent match between the closed-form solution and numerical analysis is observed. For the CFRP tool, an acceptable agreement is observed with a thermal lag of 17.8°C obtained from simulation. For this tool, thermal lag obtained from the analytical solution shows a maximum deviation of 2.4°C from the numerical solution through the entire heating cycle.

Effect of sub-structure

IR thermography results show localized cold spots coinciding with the attachment points of the sub-structure to the facesheet for the CFRP and Invar tools. The aluminum tool does not display this behaviour. This is attributed to the substructure acting as a thermal sink for these regions as a function of the thermal conductivity. The influence of thermal conductivity is better understood by deriving an analytical solution based on an energy balance for a single-finned tool in convective heating conditions.

Consider a plate with a thickness of $2L_1$ attached to a sub-structure with a thickness of $2L_2$ as shown in Figure 11. For an ambient temperature of T_∞ with a constant heating rate of r , based on the lumped mass assumption, the quasi-steady-state temperature of the plate can be calculated as follows

(Appendix 2, equation (15)):

$$T_s(x) = T_\infty - r \frac{\rho C_P (2L_1)}{h_1 + h_2} \times \left(1 + \frac{1 - \frac{h_1 + h_2}{2h_2} \times \frac{L_2}{L_1} + h_1 \sqrt{\frac{L_2}{h_2 k}}}{1 + 2\sqrt{\frac{h_1 + h_2}{2h_2}} \times \frac{L_1}{L_2} + h_1 \sqrt{\frac{L_2}{h_2 k}}} e^{-\sqrt{\frac{h_1 + h_2}{k(2L_1)}} x} \right) \quad (5)$$

where h_1 is the HTC around the plate and h_2 is the HTC around the sub-structure as shown in Figure 11. This equation can be simplified to the following format

$$T_s(x) = T_\infty - \Delta T^S \left(1 + m \times e^{-\sqrt{\frac{h_1 + h_2}{k(2L_1)}} x} \right) \quad (6)$$

where m is a constant and ΔT is the thermal lag. Equation (6) yields the same thermal lag as equation (4) when $x \rightarrow \infty$ (i.e. away from the sub-structure). However, close to the sub-structure, this thermal lag changes. Assuming the HTC around the facesheet is higher than the HTC around the sub-structure ($h_1 > h_2$) and the thickness of the facesheet and sub-structure are close ($L_1 \approx L_2$), cold spots are created above the sub-structure. Away from the sub-structure, this effect dissipates exponentially.

For given HTCs and thicknesses, the exponential term in equation (6) becomes a function of conductivity, k . Again, considering three tools with the properties listed under Table 1 and equivalent heating conditions, for a heating rate of 3°C/min and HTCs of $h_1 = 45 \text{ W/m}^2\text{K}$ and $h_2 = 15 \text{ W/m}^2\text{K}$, temperature distribution around a sub-structure is calculated using equation (6) as follows

$$\begin{cases} T_{\text{invar}} - T_\infty = -(43.6^\circ\text{C})(1 + 0.18 \times e^{-20.7x}) \\ T_{\text{aluminum}} - T_\infty = -(25.6^\circ\text{C})(1 + 0.24 \times e^{-5.3x}) \\ T_{\text{composite}} - T_\infty = -(11.9^\circ\text{C})(1 + 0.24 \times e^{-30.8x}) \end{cases} \quad (7)$$

The above analytical solution is compared with numerical results obtained from finite element simulations as shown in Figure 12. Finite element simulations were performed using the ABAQUS software package with DC2D8 heat transfer quadrilateral elements and a mesh size of 1 mm. Results from the analytical solution are found to agree well with the numerical results.

Based on equation (7), the sub-structure creates cold spots which are approximately 1.18–1.24 times more than the far field thermal lag. Because of the relatively low conductivity, this effect quickly disappears in the case of Invar and composite tools due to the

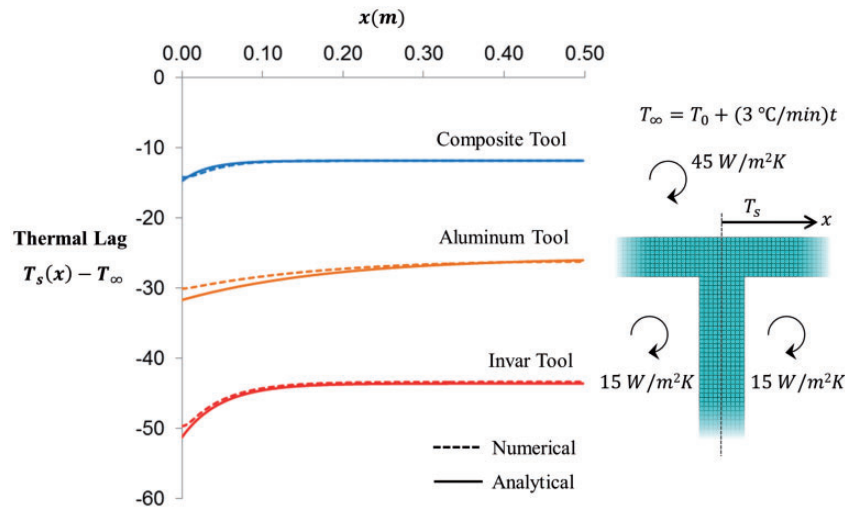


Figure 12. Comparison of the thermal lag near the sub-structure attachment for three tools with properties listed under Table 1. Thermal lag was obtained at the quasi-steady-state condition for a heating rate of 3°C/min. Numerical results were obtained for the tool surface temperature using ABAQUS software.

exponential term. For the aluminum tool, high conductivity lowers the effect of the exponential term and spreads it over a much wider region minimizing the local effect of the sub-structure and spreading its influence across a much larger region. Consequently, while the composite and Invar tools exhibit strong sub-structure effects, the aluminum tool appears to be near isothermal near the sub-structure (Figure 5).

Summary and conclusions

In this paper, an IR thermography method was presented and used to observe the thermal response of convectively heated tools. The results show a complex, non-isothermal temperature distribution not easily observed using conventional methods such as thermocouples or calorimeters. This study identifies three influencing parameters: (1) autoclave airflow variation, (2) tooling material and, (3) tooling sub-structure. By covering the tool using a painted vacuum bag and employing a proper calibration procedure, temperature measurements with acceptable accuracy were achieved. The following main observations are made using this IR thermography method in conjunction with simple analytical heat transfer models:

- Due to airflow variation in the autoclave, the HTC is not spatially constant and varies across the entire span of the tooling surface. This creates hot and cold spots on the tool surface during the heat up and entry to hold.
- For similar geometries and HTCs, the thermal mass of each tool dictates the overall temperature lag.

Invar tooling has the greatest lag and composite tooling has the lowest lag. This is supported by the presented analytical solution.

- Sub-structure effects are strongly dependent upon the material thermal conductivity. While composite and Invar tools exhibit localized cold spots coincident with the sub-structure, aluminum creates a distributed profile that effectively averages these temperature lags across the span of the tool.

This work defines the role of tooling within the broader composite curing system (equipment, tooling, part, and material). The presented methods can be used to observe and describe the thermal behaviour of complex tooling heated by convection with complex gas flow. In addition, temperature measurements from the presented full-field IR thermography methodology can be potentially used to determine the effective HTC distribution on the tool surface. Such methods can be used to support the design of the curing system with regard to choice of tooling material and geometry as well as the determination and evaluation of the effect of apparent thermal boundary conditions on a given manufacturing setup.

Acknowledgements

We would like to acknowledge many fruitful discussions with colleagues at the Composites Research Network (CRN).

Declaration of Conflicting Interests

The author(s) declared no potential conflicts of interest with respect to the research, authorship, and/or publication of this article.

Funding

The author(s) disclosed receipt of the following financial support for the research, authorship, and/or publication of this article: The authors would like to thank the Natural Sciences and Engineering Research Council of Canada (NSERC) and the industrial members of the Composites Research Network (The Boeing Company, Convergent Manufacturing Technologies, Toray Americas, Avcorp Industries) for their financial support.

ORCID iD

Navid Zobeiry  <http://orcid.org/0000-0002-3142-2682>

References

1. Fabris J, Mobuchon C, Zobeiry N, et al. Introducing thermal history producibility assessment at conceptual design. In: *SAMPE conference, society for the advancement of material and process engineering*, Baltimore, MD, 18–21 May 2015.
2. Fernlund G, Rahman N, Courdji R, et al. Experimental and numerical study of the effect of cure cycle, tool surface, geometry, and lay-up on the dimensional fidelity of autoclave-processed composite parts. *Compos Part A* 2002; 33: 341–351.
3. Johnston A, Hubert P, Fernlund G, et al. Process modeling of composite structures employing a virtual autoclave concept. *Sci Eng Compos Mater* 1996; 5: 235–252.
4. Kay J, Farhang L, Hsiao K, et al. Effect of Process conditions on porosity in out-of-autoclave prepreg laminates. In: *18th international conference on composite materials, ICCM-18*, Jeju Island, Korea, 21–26 August 2011.
5. Farhang L and Fernlund G. Void and porosity characterization of uncured and partially cured prepreps. *J Compos Mater* 2016; 50: 937–948.
6. Hallander P, Akermo M, Mattei C, et al. An experimental study of mechanisms behind wrinkle development during forming of composite laminates. *Compos Part A* 2013; 50: 54–64.
7. Zobeiry N and Poursartip A. The origins of residual stress and its evaluation in composite materials. In: Beaumont P, Soutis C and Hodzic A (eds) *Structural integrity and durability of advanced composites*. Cambridge, UK: Woodhead Publishing, 2015, pp.43–72.
8. Zobeiry N, Forghani A, Li C, et al. Multi-scale characterization and representation of composite materials during processing. *Philos Transac R Soc Lond A: Mathematical, Physical and Engineering Sciences* 2016; 374. DOI: 10.1098/rsta.2015.0278.
9. Albert C and Fernlund G. Spring-in and warpage of angled composite laminates. *Compos Sci Technol* 2002; 62: 1895–1912.
10. Telikicherla NK, Altan MC and Lai FC. Autoclave curing of thermosetting composites: process modeling for the cure assembly. *Int Commun Heat Mass Transf* 1994; 21: 785–797.
11. Hubert P, Fernlund G and Poursartip A. Autoclave processing for composites. In: Suresh Advani S and Hsiao K (eds) *Manufacturing techniques for polymer matrix composites (PMCs)*. Cambridge, UK: Woodhead Publishing, 2012, pp.414–434.
12. Dumont F, Frohlingsdorf W and Weimer C. Virtual autoclave implementation for improved composite part quality and productivity. *CEAS Aeronaut J* 2013; 15: 277–289.
13. Weber TA, Arent JC, Steffens L, et al. Thermal optimization of composite autoclave molds using the shift factor approach for boundary condition estimation. *J Compos Mater* 2017; 51: 1753–1767.
14. Kluge N, Lundstrom T, Ljung AL, et al. An experimental study of temperature distribution in an autoclave. *J Reinf Plast Compos* 2016; 35: 566–578.
15. Park J, Zobeiry N and Poursartip A. Tooling materials and their effect on surface thermal gradients. In: *SAMPE conference, society for the advancement of material and process engineering*, Seattle, WA, 22–25 May 2017.
16. Bergman TL, Lavine AS, Incropera FP, et al. *Fundamentals of heat and mass transfer*. New Jersey, USA: John Wiley & Sons, 2017.
17. Ghariban N, Lou DYS and Haji-Singh A. Effect of honeycomb flow straighteners on turbulence and heat transfer in autoclave model. In: Guceri SI and Alam MK (eds) *Heat transfer effects in materials processing, proceedings of ASME winter annual meeting*. New York City, USA, 1992, HTD 233, pp. 45–52.
18. Johnston A, Hubert P, Fernlund G, et al. Process modeling of composite structures employing a virtual autoclave concept. *Sci Eng Compos Mater* 1996; 5: 235–252.
19. Hudek M, Shewfelt M, Shead RM, et al. Examination of heat transfer in autoclaves. In: *46th international SAMPE symposium and exhibition*, Long Beach, CA, 6–10 May 2001.
20. Weber TA, Arent JC, Münch L, et al. A fast method for the generation of boundary conditions for thermal autoclave simulation. *Compos Part A* 2016; 88: 216–225.
21. Maffezzoli A and Grieco A. Optimization of parts placement in autoclave processing of composites. *Appl Compos Mater* 2013; 20: 233–248.
22. Carlomagno GM and Cardone G. Infrared thermography for convective heat transfer measurements. *Exp Fluids* 2010; 49: 1187–1218.
23. Goidescu C, Weleman H, Garnier C, et al. Damage investigation in CFRP composites using full-field measurement techniques: combination of digital image stereo-correlation, infrared thermography and X-ray tomography. *Compos Part B* 2013; 48: 95–105.
24. Liebers N, Ucan H, Kleiberg M, et al. Sensor and real-time-process-simulation guided autoclave process control for composite production. In: *28th international congress of the aeronautical sciences*, Brisbane, Australia, 23–28 September 2012.
25. Tripmaker A and Ucan H. Detection of leakages on composite high performance structure parts. *Lightweight Des Worldwide* 2017; 10: 46–49.
26. Borhade N, Akin D and Ucan H. Optimization of autoclave process through design, development and validation of thermographic feedback system & monitoring application for a networked heating control system, Report no.

- DLR-IB-FA-SD-2016-122, 81 S. German Aerospace Center, 2016.
27. Ucan H, Akin D, Tripmaker A, et al. Einsatzmöglichkeiten von Thermographiemessungen im Autoklaven zur qualitätsgesicherten Fertigung von CFK-Bauteilen. In: *Deutscher Luft- und Raumfahrt Kongress*, Rostock, Germany, 22–24 September 2015.
 28. Hubert P. *Aspects of flow and compaction of laminated composite shapes during cure*. Doctoral Dissertation, University of British Columbia, Canada, 1996.
 29. Davis JR. *Metals handbook desk edition*. Milton Park, Didcot, UK: ASM International, Handbook Committee, Taylor & Francis, 1998.
 30. Convergent Manufacturing Technologies. RAVEN simulation software, www.convergent.ca/products/raven-simulation-software (2013, accessed 13 February 2018).
 31. Slesinger N, Shimizu T, Arafath ARA, et al. Heat transfer coefficient distribution inside an autoclave. In: *17th international conference on composite materials, ICCM-17*, Edinburgh, UK, 27–31 July 2009.
 32. Usamentiaga R, Venegas P, Guerediaga J, et al. Infrared thermography for temperature measurement and non-destructive testing. *Sensors* 2014; 14: 12305–12348.
 33. FLIR Systems. *The ultimate infrared handbook for R&D professionals*. Oregon, USA: FLIR AB, 2015.
 34. Vollmer M and Möllmann K. *Infrared thermal imaging: fundamentals, research and applications*. New Jersey, USA: John Wiley & Sons, 2010.
 35. Minkina W and Dudzik S. *Infrared thermography: errors and uncertainties*. New Jersey, USA: John Wiley & Sons, 2009.

Based on the lumped mass assumption, for 1D heat transfer through the thickness of a slab and using the thermal energy balance of a unit width, we can write

$$\dot{E}_{st} = \dot{E}_{in} \rightarrow 2L\rho C_P \frac{dT}{dt} = (h_1 + h_2)(T_\infty - T) \quad (8)$$

For the heat-up step

$$\begin{cases} \frac{2\rho C_P L}{h_1 + h_2} \frac{dT_1}{dt} = T_0 + rt - T_1 \\ T_1(0) = T_0 \end{cases} \rightarrow \begin{cases} T_1(t) = T_\infty - \Delta T^S (1 - e^{\frac{-rt}{\Delta T^S}}) \\ \Delta T^S = r \frac{\rho C_P (2L)}{h_1 + h_2} \end{cases}, t < t_{hold} \quad (9)$$

where ΔT is the quasi-steady-state lag as shown in Figure 8. For the hold segment

$$\begin{cases} \frac{2\rho C_P L}{h_1 + h_2} \frac{dT_2}{dt} = T_{hold} - T_2 \\ T_2(t_{hold}) = T_1(t_{hold}) \end{cases} \rightarrow \begin{cases} T_2(t) = T_{hold} \\ - (T_{hold} - T_1(t_{hold})) e^{\frac{-r}{\Delta T^S}(t - t_{hold})}, t > t_{hold} \end{cases} \quad (10)$$

Equations (9) and (10) can be summarized as follows

Appendix I

$T_s(x), T_f(y)$	Average temperatures of slab and fin as shown in Figure 11
$2L_1, 2L_2$	Thickness of the slab and fin respectively as shown in Figure 11
h_1, h_2	Heat transfer coefficients as shown in Figure 11
k	In-plane thermal conductivity
T_1, T_2	Average temperatures of a slab during $t < t_{hold}$ and $t > t_{hold}$
$T_\infty = T_0 + rt$	Ambient temperature, T_∞ , initial temperature, T_0 , and heating rate, r
T_{hold}, t_{hold}	Hold temperature and hold time as shown in Figure 8
$2L$	Thickness as shown in Figure 8
ΔT^S	Quasi steady-state thermal lag as shown in Figure 8
$\dot{E}_{st}, \dot{E}_{in}$	Rate of stored and inflow thermal energy respectively
ρC_P	Density \times specific heat capacity
h_1, h_2	Heat transfer coefficients as shown in Figure 8

$$T(t) = \begin{cases} T_0 + rt - \Delta T^S (1 - e^{\frac{-rt}{\Delta T^S}}), t < t_{hold} \\ T_{hold} - \Delta T^S (e^{\frac{-r}{\Delta T^S}(t - t_{hold})} - e^{\frac{-rt}{\Delta T^S}}), t > t_{hold} \end{cases}$$

$$\Delta T^S = r \frac{\rho C_P (2L)}{h_1 + h_2} \quad (11)$$

Appendix 2

Using the lumped mass assumption and based on the thermal energy balance, we can write the following equations for the slab and fin depicted in Figure 11

$$\begin{cases} k \frac{\partial^2 T_s}{\partial x^2} - \frac{h_1 + h_2}{2L_1} (T_s - T_\infty) = \rho C_P \frac{\partial T_s}{\partial t} \\ k \frac{\partial^2 T_f}{\partial y^2} - \frac{2h_2}{2L_2} (T_f - T_\infty) = \rho C_P \frac{\partial T_f}{\partial t} \end{cases} \quad (12)$$

$$\begin{cases} U_s = T_s - T_\infty = T_s - T_0 - rt \\ U_f = T_f - T_\infty = T_f - T_0 - rt \end{cases}$$

$$\rightarrow \begin{cases} \frac{\partial^2 U_s}{\partial x^2} - \frac{h_1 + h_2}{2kL_1} U_s = \frac{\rho C_P}{k} \left(r + \frac{\partial U_s}{\partial t} \right) \\ \frac{\partial^2 U_f}{\partial y^2} - \frac{2h_2}{2kL_2} U_f = \frac{\rho C_P}{k} \left(r + \frac{\partial U_f}{\partial t} \right) \end{cases} \quad (13)$$

For steady-state condition, the following sets of equations should be solved

$$\begin{cases} \frac{d^2 U_s}{dx^2} - \frac{h_1 + h_2}{2kL_1} U_s = r \frac{\rho C_P}{k} \\ \frac{d^2 U_f}{dy^2} - \frac{2h_2}{2kL_2} U_f = r \frac{\rho C_P}{k} \end{cases}$$

$$\& \begin{cases} k \frac{dU_s}{dx} \Big|_{x \rightarrow \infty} = 0 \\ k \frac{dU_f}{dy} \Big|_{y \rightarrow \infty} = 0 \\ U_s(0) = U_f(0) \\ 2L_1 k \frac{dU_s}{dx} \Big|_{x=0} + kL_2 \frac{dU_f}{dy} \Big|_{y=0} - h_1 L_2 U_s(0) = 0 \end{cases} \quad (14)$$

The location for heat flux balance is marked as point A in Figure 11. From this set of equations, the temperature distribution of the slab along the x-direction can be calculated

$$T_s(x) = T_\infty - r \frac{\rho C_P (2L_1)}{h_1 + h_2} \times \left(1 + \frac{1 - \frac{h_1 + h_2}{2h_2} \times \frac{L_2}{L_1} + h_1 \sqrt{\frac{L_2}{h_2 k}}}{1 + 2\sqrt{\frac{h_1 + h_2}{2h_2}} \times \frac{L_1}{L_2} + h_1 \sqrt{\frac{L_2}{h_2 k}}} e^{-\sqrt{\frac{h_1 + h_2}{k(2L_1)}} x} \right) \quad (15)$$